Int. J. Heat Mass Transfer. Vol. 36, No. 15, pp. 3841–3850, 1993
Printed in Great Britain

0017–9310/93 $6.00 + 0.00

Forced convection on a rotating cylinder with an incident air jet

C. C. CHIOU and S. L. LEE

Department of Power Mechanical Engineering, National Tsing-Hua University, Hsinchu 30043, Taiwan, R.O.C.

(*Received* 9 *September* 1992 *and in final form* 18 *February* 1993)

Abstract—Forced convection on a rotating cylinder cooled with an air jet is investigated in the present study. To properly handle the jet flow before and after hitting the cylinder, a computational domain having an irregular shape is employed. Results of streamlines, isotherms and Nusselt numbers are presented for jet Reynolds numbers of $Re_j = 100$, 500 and 1000 under various rotation Reynolds numbers in the range of $0 \leqslant Re_\omega/Re_j \leqslant 1$. It is interesting to find two solution modes in the present problem. For small rotation speeds, the jet flow is separated into two branches upon hitting the cylinder. Each branch has a separation point. With the aid of the rotating cylinder, one of the separation points moves downstream, while the other receives little influence. Hence, the overall heat transfer is enhanced. For high rotation speeds, however, this heat transfer behavior is reversed due to a layer of dead air round the cylinder. Nevertheless, a more uniform heat transfer is achieved. For both cases of $Re_j = 500$ and 1000, dual solutions according to each of the two solution modes exist in a range of rotation Reynolds numbers. Like the transition from laminar to turbulent flow, the heat transfer characteristics jump from one solution mode to the other depending on the flow instability. However, the transition between the two solution modes is not clear for a jet Reynolds number Re_j as small as 100.

INTRODUCTION

CONVECTIVE heat transfer from a rotating cylinder has numerous applications in thermal engineering such as cooling of rotating machinery, design of rotating heat exchangers, drying of paper, etc. Hence, many theoretical and experimental works have been conducted to study this particular problem over the past decades. Among the early studies, the experiments [1, 2] showed that the rotating speed of a horizontal heated cylinder had a critical value, below which the heat transfer was essentially insensitive to the rotating speed. Beyond the critical value, the heat transfer increased approximately in the 2/3 power of the rotation speed. The existence of the critical rotation speed was attributed to the onset of turbulence. However, Etemad's experiment [3] indicated that this was due to the development of a three-dimensional secondary flow. The onset of turbulence would occur at a rotation speed much higher than the critical speed. Etemad [3] also found that as long as the rotation speed was maintained below the critical value, the heat transfer coefficient would decrease slightly due to the thicker boundary layer around the cylinder when the rotation speed increased. Etemad's findings were verified by Farouk and Ball's experiment and numerical simulation [4] some 30 years later.

The experiment of Kays and Bjorklund [5] is one of the earliest studies that investigated heat transfer from a rotating cylinder with cross-flow. The rotation Reynolds number Re_ω in this experiment was in the range 2000–45 000. Under such a high rotation Reynolds number, Kays and Bjorklund found two flow regimes depending on the ratio of the rotation Reynolds number Re_ω and the free stream Reynolds number Re_s. When $Re_\omega/Re_s < 2$, the boundary layer separated in a manner similar to that of the non-rotating cylinder. However, when the rotation speed was increased such that $Re_\omega/Re_s > 2$, there was a layer of dead air wound around the cylinder due to the high rotation speed of the cylinder. As a result, the flow separation disappeared and the heat transfer characteristic transited from the free stream dominated regime to the rotation dominated regime. Similar phenomena were observed by Jones *et al.* [6].

It should be noted here that the rotation Reynolds numbers employed in the experiments of refs. [5, 6] were beyond the critical value [1–4]. Hence, in the rotation dominated regime ($Re_\omega/Re_s > 2$), the heat transfer coefficient increased as the rotation speed increased. However, this would not be true for a rotation speed below the critical value. Recently, Badr and Dennis [7] studied this same flow configuration numerically. The considered parameters were $5 \leqslant Re_s \leqslant 100$ and $0.1 \leqslant Re_\omega/Re_s \leqslant 4$. This implied a rotation Reynolds number in the range of $0.5 \leqslant Re_\omega \leqslant 400$, which was below the critical value. Their results revealed that the average Nusselt number increased when the free stream Reynolds number Re_s increased, in spite of the rotation speed. When the rotation speed increased, however, the average Nusselt number always decreased as in the case of no cross-flow [3, 4]. The heat transfer characteristic did

Correspondence to: Dr Shong-Leih Lee, Department of Power Mechanical Engineering, National Tsing-Hua University, Hsinchu 30043, Taiwan, R.O.C.

NOMENCLATURE

a weighting factors of discretized equations (31)
B a general function used in equations (29) and (32)
D diameter of the cylinder [m]
E width of the nozzle exit [m]
Gr Grashof number, $\beta g \Delta T D^3/\nu^2$
g gravity, 9.81 m s^{-2}
J Jacobian, $x_\xi y_\eta - x_\eta y_\xi$
L distance from the nozzle exit to the cylinder surface [m]
$Nu, \overline{Nu}$ local Nusselt number and average Nusselt number, see equations (38) and (39)
P static pressure [N m^{-2}]
p dimensionless pressure, $P/(\rho U_j^2)$
Pe Peclet number, $Pr\ Re_j$
Pr Prandtl number, ν/α
Re_j jet Reynolds number, $U_j D/\nu$
Re_ω rotation Reynolds number, $\omega D^2/(2\nu)$
s_η $\Delta s/\Delta\eta$
T_0, T_∞ temperatures of the cylinder and the ambient air [K]
U, V dimensionless velocities defined in equations (14)
u, v dimensionless velocities, U^*/U_j and V^*/U_j
U^*, V^* velocity components in X and Y directions [m s^{-1}]
$w_f(Z), w_f^*(Z)$ weighting functions defined in equations (33)
X, Y coordinate system defined in Fig. 1 [m]
x, y dimensionless coordinates, X/D and Y/D
Z parameter of the weighting functions.

Greek symbols
α thermal diffusivity of the air [m^2 s^{-2}] or geometry parameter defined in equations (14)
β thermal expansion coefficient of the air [K^{-1}] or geometry parameter defined in equations (14)
γ geometry parameter defined in equations (14)
Δ difference quantity or step size of the grid system
ΔT temperature difference, $T_0 - T_\infty$ [K]
Δs stand-off spacing between $\eta = 0$ and $\eta = \Delta\eta$
ζ dimensionless vorticity, $v_x - u_y$
η curvilinear coordinate
θ dimensionless temperature, $(T - T_\infty)/(T_0 - T_\infty)$
λ ratio of rotation and jet Reynolds numbers, Re_ω/Re_j or $\omega D/(2U_j)$
ν kinematic viscosity [m^2 s^{-1}]
ξ curvilinear coordinate
ξ^* a range of ξ denoting the location of the nozzle exit
ξ_0 location of the nozzle center
ρ density of the air [kg m^{-3}]
Φ a general function used in equation (29)
ϕ angle measured from positive X-axis, see Fig. 1
ψ stream function, $u = \psi_y$ and $v = -\psi_x$
ψ_0 stream function at the center of nozzle exit.

Superscripts
$\tilde{}$ guessed quantity.

Subscripts
E, N, S, W, P quantity at points E, N, S, W and P
e, n, s, w quantity at the interface points (e, n, s, w) of control volume P
x, y, ξ, η differentiations with respect to x, y, ξ and η, respectively.

not transit from the rotation dominated regime to the free stream dominated regime even though the value of Re_ω/Re_s was well below 2. This phenomenon is entirely different from the finding reported by Kays and Bjorklund [5] for a case having a rotation Reynolds number beyond the critical value.

In many applications, rotating an object is only to ensure a uniform cooling (to avoid thermal deformation) rather than to obtain a higher cooling rate. For this purpose, the rotation Reynolds number is usually below the critical value. Generally speaking, cooling an object by using a jet is more practical than using a uniform cross-flow. However, the jet flow would reflect when it hits the object. Hence, its cooling performance could be quite different from that of a uniform cross-flow. The work of Zhang *et al.* [8] seems to be the only publication in the literature that studied the cooling of a rotating cylinder with an air jet. Unfortunately, Zhang *et al.* measured only the average Nusselt number. No attempt was undertaken to study the flow field. In addition, their measurement was not sufficiently precise to detect the effect of the rotation Reynolds number on the average Nusselt number. The purpose of the present study is to investigate the flow field and heat transfer numerically for a rotating cylinder with an incident air jet. Such a flow field has not been studied in the past.

THEORETICAL ANALYSIS

Consider a cylinder of diameter D rotating counterclockwise in a quiescent air with an angular rotation

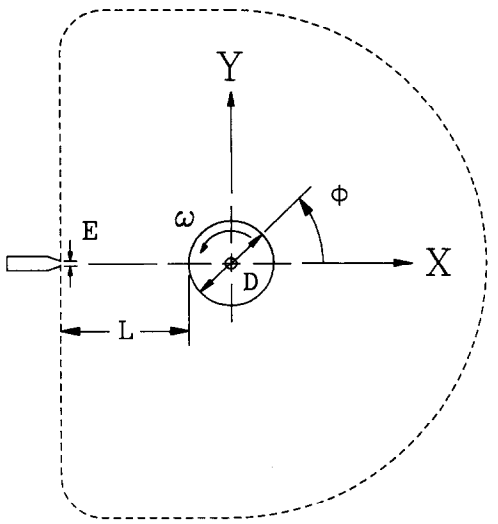

FIG. 1. Schematic configuration of the problem and the coordinate system.

speed ω. A laminar air jet with a uniform velocity U_j blows from a two-dimensional nozzle toward the center of the rotating cylinder as shown in Fig. 1. Let the nozzle width and the distance from the nozzle exit to the cylinder surface be denoted by E and L, respectively. The surface temperature of the rotating cylinder T_0 is assumed to be uniform as suggested by Zhang *et al.* [8], while both the ambient air and the air from the nozzle have the same temperature T_∞. In the present study, the interaction of the air jet and the rotating cylinder is emphasized. Hence, the temperature difference $\Delta T = T_0 - T_\infty$ is assumed sufficiently small such that the natural convection is negligible and all of the thermophysical properties of the air are constant.

In the present study, the computational domain is defined by the dashed curve shown in Fig. 1. For convenience, the dashed curve will be referred to as the 'outer boundary'. The origin of the coordinate system (X, Y) is located at the center of the cylinder, while the angle ϕ is measured from the positive X-axis. Unlike the cross-flow case, the jet might reflect after hitting the rotating cylinder. Thus, wake flow is not necessary to exist behind the cylinder. For this reason, the outer boundary in the region $X \geqslant 0$ is defined by a half-circle of diameter $6D$. To properly handle the nozzle, however, a vertical straight line at $X = -(L + D/2)$ is employed as a part of the outer boundary.

After introducing the dimensionless transformation

$$u = U^*/U_j, \quad v = V^*/U_j, \quad x = X/D, \quad y = Y/D,$$
$$p = P/(\rho U_j^2), \quad \theta = (T - T_\infty)/(T_0 - T_\infty) \tag{1}$$

the governing equations are expressible as

$$\frac{\partial u}{\partial x} + \frac{\partial v}{\partial y} = 0 \tag{2}$$

$$u\frac{\partial u}{\partial x} + v\frac{\partial u}{\partial y} = -\frac{\partial p}{\partial x} + \frac{1}{Re_j}\left(\frac{\partial^2 u}{\partial x^2} + \frac{\partial^2 u}{\partial y^2}\right) \tag{3}$$

$$u\frac{\partial v}{\partial x} + v\frac{\partial v}{\partial y} = -\frac{\partial p}{\partial y} + \frac{1}{Re_j}\left(\frac{\partial^2 v}{\partial x^2} + \frac{\partial^2 v}{\partial y^2}\right) \tag{4}$$

$$u\frac{\partial \theta}{\partial x} + v\frac{\partial \theta}{\partial y} = \frac{1}{Pe}\left(\frac{\partial^2 \theta}{\partial x^2} + \frac{\partial^2 \theta}{\partial y^2}\right) \tag{5}$$

subject to the associated boundary conditions

on the surface of the cylinder

$$u = -\lambda \sin\phi, \quad v = \lambda \cos\phi, \quad \theta = 1 \tag{6}$$

at the nozzle exit

$$u = 1, \quad v = 0, \quad \theta = 0 \tag{7}$$

on the outer boundary of the computational domain

$$\frac{\partial u}{\partial x} = \frac{\partial u}{\partial y} = \frac{\partial v}{\partial x} = \frac{\partial v}{\partial y} = 0, \quad \theta = 0 \tag{8}$$

where $Re_j = U_j D/\nu$ is the Reynolds number of the jet, and $Pe = Pr\,Re_j$ is the Peclet number. The symbol $\lambda = \omega D/(2U_j) = Re_\omega/Re_j$ denotes the dimensionless moving speed of the cylinder surface. As mentioned earlier, the air jet could go across the outer boundary after hitting the cylinder. Under such a situation, the velocity on the outer boundary is very difficult to define. Nevertheless, it is reasonable to assume that the reflected jet just goes straight forward when it enters a region near the outer boundary. This is the major reason for the use of equations (8). In the present analysis, the flow is assumed two-dimensional and steady-state. Hence, the governing equations can be greatly simplified by eliminating the pressure from equations (3) and (4). This leads to

$$\frac{\partial^2 \psi}{\partial x^2} + \frac{\partial^2 \psi}{\partial y^2} = -\zeta \tag{9}$$

$$u\frac{\partial \zeta}{\partial x} + v\frac{\partial \zeta}{\partial y} = \frac{1}{Re_j}\left(\frac{\partial^2 \zeta}{\partial x^2} + \frac{\partial^2 \zeta}{\partial y^2}\right) \tag{10}$$

where $\zeta = \partial v/\partial x - \partial u/\partial y$ is the vorticity. The stream function ψ is defined such that $u = \partial\psi/\partial y$ and $v = -\partial\psi/\partial x$.

Next, make a branch-cut along $\phi = 0$ and generate an O-type body-fitted coordinate system (ξ, η) with a uniform step size $\Delta\xi = \Delta\eta = 1$ by using a Poisson grid generation method proposed in ref. [9]. Figure 2 shows the resulting grid system in the xy-plane, where the diameter of the cylinder is unity. Thanks to the use of this particular grid generation technique, the boundary grids are properly controlled. As observable from Fig. 2, small orthogonal grids are generated around the cylinder as desired, while those on the outer boundary are all orthogonal. Through the coordinate transformation from the xy-plane to the $\xi\eta$-plane, the physical domain (see Fig. 2) is mapped to the rectangular region $0 \leqslant \xi \leqslant \xi_{max}$ and $0 \leqslant \eta \leqslant \eta_{max}$. The cylinder surface corresponds to the bottom side

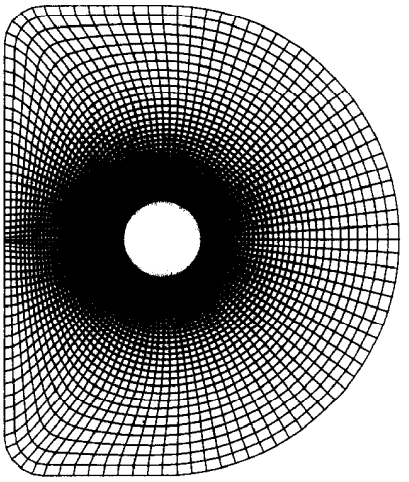

FIG. 2. The O-type grid system for the computational domain.

of the rectangle ($\eta = 0$ and $0 \leqslant \xi \leqslant \xi_{max}$), while the outer boundary becomes the top side ($\eta = \eta_{max}$, $0 \leqslant \xi \leqslant \xi_{max}$). The branch-cut separates the line $\phi = 0$ into the two vertical sides $\xi = 0$ and $\xi = \xi_{max}$ of the rectangle.

On the curvilinear coordinate system (ξ, η), the governing equations (9), (10) and (5), respectively, are

$$\frac{\partial}{\partial\xi}\left(\frac{\alpha}{J}\frac{\partial\psi}{\partial\xi}\right)+\frac{\partial}{\partial\eta}\left(\frac{\gamma}{J}\frac{\partial\psi}{\partial\eta}\right)-\frac{\partial}{\partial\xi}\left(\frac{\beta}{J}\frac{\partial\psi}{\partial\eta}\right)-\frac{\partial}{\partial\eta}\left(\frac{\beta}{J}\frac{\partial\psi}{\partial\xi}\right)=-J\zeta \quad (11)$$

$$\frac{\partial}{\partial\xi}(Re_j U\zeta)+\frac{\partial}{\partial\eta}(Re_j V\zeta)=\frac{\partial}{\partial\xi}\left(\frac{\alpha}{J}\frac{\partial\zeta}{\partial\xi}\right)+\frac{\partial}{\partial\eta}\left(\frac{\gamma}{J}\frac{\partial\zeta}{\partial\eta}\right)-\frac{\partial}{\partial\xi}\left(\frac{\beta}{J}\frac{\partial\zeta}{\partial\eta}\right)-\frac{\partial}{\partial\eta}\left(\frac{\beta}{J}\frac{\partial\zeta}{\partial\xi}\right) \quad (12)$$

$$\frac{\partial}{\partial\xi}(Pe\,U\theta)+\frac{\partial}{\partial\eta}(Pe\,V\theta)=\frac{\partial}{\partial\xi}\left(\frac{\alpha}{J}\frac{\partial\theta}{\partial\xi}\right)+\frac{\partial}{\partial\eta}\left(\frac{\gamma}{J}\frac{\partial\theta}{\partial\eta}\right)-\frac{\partial}{\partial\xi}\left(\frac{\beta}{J}\frac{\partial\theta}{\partial\eta}\right)-\frac{\partial}{\partial\eta}\left(\frac{\beta}{J}\frac{\partial\theta}{\partial\xi}\right) \quad (13)$$

where the parameters α, β, γ, J, U and V are defined by

$$\alpha = x_\eta^2+y_\eta^2, \quad \beta = x_\xi x_\eta + y_\xi y_\eta,$$
$$\gamma = x_\xi^2+y_\xi^2, \quad J = x_\xi y_\eta - x_\eta y_\xi,$$
$$U = uy_\eta - vx_\eta = \psi_\eta, \quad V = vx_\xi - uy_\xi = -\psi_\xi \quad (14)$$

with the subscripts 'ξ' and 'η' standing for partial differentiation with respect to ξ and η. It should be noted that there are two boundary conditions for the stream function, while the vorticity boundary condition is lacking. Hence, a particular treatment is needed to achieve good numerical stability.

On the cylinder surface ($\eta = 0$), the boundary conditions (6) imply

$$\psi_\xi = -\lambda(x_\xi\cos\phi + y_\xi\sin\phi) \quad (15)$$

$$\psi_\eta = -\lambda(y_\eta\sin\phi + x_\eta\cos\phi) \quad (16)$$

where $\phi = \phi(\xi)$ having the boundary values $\phi(0) = 2\pi$ and $\phi(\xi_{max}) = 0$. From the geometry relationship around the cylinder surface ($x = \cos\phi$ and $y = \sin\phi$), one obtains

$$x_\xi = -\sin\phi\,\phi_\xi \quad \text{and} \quad y_\xi = \cos\phi\,\phi_\xi. \quad (17)$$

This implies $\psi_\xi = 0$ from equation (15), such that the stream function ψ has a constant value on the cylinder surface. In the present study, this constant is assigned zero for simplicity, i.e.

$$\psi(\xi, 0) = 0. \quad (18)$$

As mentioned earlier, the present body-fitted coordinates system (Fig. 2) has orthogonal grids around the cylinder surface. In addition, the 'stand-off' spacing Δs between the two curves $\eta = 0$ and $\eta = \Delta\eta$ is constant ($\Delta s = 0.01$ in the present study) around the cylinder surface [9]. Based on these, equation (16) is rewritten as

$$\psi_\eta(\xi, 0) = -\lambda s_\eta = \text{constant} \quad (19)$$

where $s_\eta = (x_\eta^2+y_\eta^2)^{1/2} = \Delta s/\Delta\eta$. The vorticity boundary condition $\zeta(\xi, 0)$ can be obtained from the governing equation (11) by applying the properties of orthogonal boundary grid ($\beta = 0$) and equations (18) and (19). This yields

$$\zeta(\xi, 0) = -\frac{1}{J}\frac{\partial}{\partial\eta}\left(\frac{\gamma}{J}\frac{\partial\psi}{\partial\eta}\right) = \lambda s_\eta\frac{1}{J}\frac{\partial}{\partial\eta}\left(\frac{\gamma}{J}\right)-\frac{\gamma}{J^2}\psi_{\eta\eta}. \quad (20)$$

On the nozzle exit, equations (7) are expressible as

$$\psi_\xi = y_\xi \quad (21)$$

$$\psi_\eta = 0. \quad (22)$$

Thus, the boundary condition of the stream function across the nozzle exit can be evaluated from

$$\psi(\xi^*, \eta_{max}) = \psi_0 + y \quad (23)$$

where ξ^* is in a range of ξ-values corresponding to the location of the nozzle. The symbol ψ_0 denotes the stream function at the center of the nozzle. Its value is not known a priori and will be determined as part of the solution. As on the cylinder surface, the vorticity at the nozzle exit can be derived from equation (11) with the properties of $\beta = 0$ and equations (22) and (23). Hence

$$\zeta(\xi^*, \eta_{max}) = -\frac{1}{J}\left[\frac{\partial}{\partial\xi}\left(\frac{\alpha}{J}y_\xi\right)+\frac{\gamma}{J}\psi_{\eta\eta}-y_\xi\frac{\partial}{\partial\eta}\left(\frac{\beta}{J}\right)\right]. \quad (24)$$

On the outer boundary, equations (8) imply

$$\zeta(\xi, \eta_{max}) = 0 \quad (25)$$

$$\psi_{\xi} = \text{constant} \quad (26)$$

$$\psi_{\eta} = \text{constant}. \quad (27)$$

It should be noted that equations (26) and (27) provide no help in defining the stream function. Furthermore, they cannot be used simultaneously. Due to the lack of further reliable information, the simple boundary condition

$$\psi_{\eta}(\xi, \eta_{max}) = 0 \quad (28)$$

is employed. Fortunately, the outer boundary is located at the downstream of the jet flow. In addition, the temperature gradient near the outer boundary is essentially zero. Hence, the use of equation (28) is expected not to have a significant influence on the flow field and heat transfer in a region near the cylinder. Finally, the boundary conditions at $\xi = 0$ and $\xi = \xi_{max}$ are treated as periodic conditions, because they correspond to the same location (the branch-cut $\phi = 0$) in the physical domain.

SOLUTION METHOD

The governing equations (11) and (12) along with the associated boundary conditions (18), (20), (23), (24), (25) and (28) constitute a system of partial differential equations. Once this system of equations is solved, the velocity is evaluated from the stream function $\psi(\xi, \eta)$. With the velocity result, the temperature $\theta(\xi, \eta)$ can be determined by solving the energy equation (13) and the associated boundary conditions (6)–(8).

Note that all of equations (11)–(13) possess the general form

$$\frac{\partial}{\partial \xi}(A\Phi) + \frac{\partial}{\partial \eta}(B\Phi) = \frac{\partial}{\partial \xi}\left(\frac{\alpha}{J}\frac{\partial \Phi}{\partial \xi}\right) + \frac{\partial}{\partial \eta}\left(\frac{\gamma}{J}\frac{\partial \Phi}{\partial \eta}\right) - \frac{\partial}{\partial \xi}\left(\frac{\beta}{J}\frac{\partial \Phi}{\partial \eta}\right) - \frac{\partial}{\partial \eta}\left(\frac{\beta}{J}\frac{\partial \Phi}{\partial \xi}\right) + JS. \quad (29)$$

Applying the weighting function scheme [9, 10] on equation (29) for grid point P of a uniform grid system ($\Delta\xi = \Delta\eta = 1$), one obtains the algebraic equation

$$a_{SW}\Phi_{SW} + a_W\Phi_W + a_{NW}\Phi_{NW} + a_S\Phi_S + a_P\Phi_P + a_N\Phi_N + a_{SE}\Phi_{SE} + a_E\Phi_E + a_{NE}\Phi_{NE} = a_R \quad (30)$$

$$a_W = \left(\frac{\alpha}{J}\right)_w w_f(Z_w), \quad a_E = \left(\frac{\alpha}{J}\right)_e w_f(-Z_e)$$

$$a_S = \left(\frac{\gamma}{J}\right)_s w_f(Z_s), \quad a_N = \left(\frac{\gamma}{J}\right)_n w_f(-Z_n)$$

$$a_P = -a_W - a_E - a_S - a_N, \quad a_R = -JS$$

$$a_{SW} = -2\left(\frac{\beta}{J}\right)_{sw} w_f^*(Z_s) w_f^*(Z_w)$$

$$a_{NW} = 2\left(\frac{\beta}{J}\right)_{nw} w_f^*(Z_n) w_f^*(Z_w)$$

$$a_{SE} = 2\left(\frac{\beta}{J}\right)_{se} w_f^*(Z_s) w_f^*(Z_e)$$

$$a_{NE} = -2\left(\frac{\beta}{J}\right)_{ne} w_f^*(Z_n) w_f^*(Z_e) \quad (31)$$

$$Z_w = (AJ/\alpha)_w, \quad Z_e = (AJ/\alpha)_e$$

$$Z_s = (BJ/\gamma)_s, \quad Z_n = (BJ/\gamma)_n \quad (32)$$

where the subscript W denotes quantity at point W (the nearest point lies to the west of point P), while w stands for the middle point of $\overline{WP}$. Points E, S and N have similar definitions with E, S and N representing east, south and north, respectively. Such a notation system has been widely used in the literature. It is interesting to note that the weighting function scheme was developed from a locally analytical solution. This particular scheme produces an exact solution for any homogeneous ordinary differential equation with constant coefficients. It thus possesses no truncation error, although other modes of errors could arise when the coefficients are not constant or when it is applied on a multidimensional problem.

In the present study, a quantity at a point other than the grid points is estimated by linearly interpolating from the known quantities. For example, let $(\alpha/J)_w = [(\alpha/J)_W + (\alpha/J)_P]/2$ and $2(\beta/J)_{sw} = (\beta/J)_S + (\beta/J)_W$, etc. The weighting functions appearing in equations (31) can be evaluated from

$$w_f(Z) = [0, (1 - 0.1|Z|)^5] + [0, Z]$$

$$w_f^*(Z) = (2 + 0.3332Z^2 + 0.0172Z^4)^{-1} \quad (33)$$

where $[a, b]$ denotes the greater of a and b. For the stream function equation (11), the weighting factors reduce to

$$a_W = \left(\frac{\alpha}{J}\right)_w, \quad a_E = \left(\frac{\alpha}{J}\right)_e, \quad a_S = \left(\frac{\gamma}{J}\right)_s, \quad a_N = \left(\frac{\gamma}{J}\right)_n$$

$$a_{SW} = -\left(\frac{\beta}{J}\right)_{sw}/4, \quad a_{NW} = \left(\frac{\beta}{J}\right)_{nw}/4$$

$$a_{SE} = \left(\frac{\beta}{J}\right)_{se}/4, \quad a_{NE} = -\left(\frac{\beta}{J}\right)_{ne}/4 \quad (34)$$

due to the properties $A = B = 0$ and thus $w_f(0) = 1$, $w_f^*(0) = 0.5$.

It should be noted that on the cylinder surface, $\psi = 0$ and $\psi_{\eta} = -\lambda s_{\eta}$. Based on a parabolic interpolation curve, the value of $\psi_{\eta\eta}$ in the boundary condition (20) can be updated from

$$\psi_{\eta\eta} = 2(\tilde{\psi} + \lambda s_{\eta}) \quad (35)$$

during the iterations, where $\tilde{\psi}$ represents the $\psi(\xi, \Delta\eta)$ result of the previous iteration. Similarly, the $\psi_{\eta\eta}$ value on the nozzle exit (24) can be estimated from

$$\psi_{nn} = 2(\tilde{\psi}_2 - \tilde{\psi}_1) \tag{36}$$

where $\psi_\eta = 0$ has been assigned and $\tilde{\psi}_1 = \psi(\xi^*, \eta_{\max})$ and $\tilde{\psi}_2 = \psi(\xi^*, \eta_{\max} - \Delta\eta)$ are obtained from the result of the previous iteration. Also, from the boundary condition $\psi_\eta = 0$, the ψ_0 value in equation (23) is simply assigned as

$$\psi_0 = \tilde{\psi}(\xi_0, \eta_{\max} - \Delta\eta) \tag{37}$$

where ξ_0 denotes the location of the center of the nozzle exit.

Thanks to the orthogonal boundary grids on the cylinder surface, the local Nusselt number $Nu(\phi)$ and the average Nusselt number $\overline{Nu}$ can be simply evaluated from

$$Nu(\phi) = -\theta_\eta(\xi, 0)/s_\eta \tag{38}$$

$$\overline{Nu} = \frac{1}{2\pi}\int_0^{2\pi} Nu(\phi)\,\mathrm{d}\phi \tag{39}$$

once the temperature solution is available.

RESULTS AND DISCUSSION

Numerical results for stream functions, temperature distributions and Nusselt numbers were obtained for jet Reynolds numbers of $Re_j = 100$, 500 and 1000, subject to the Prandtl number of 0.7 and various rotation Reynolds numbers in the range $0 \leqslant Re_\omega/Re_j \leqslant 1$. The width of the nozzle E/D is 0.3, while the distance from the nozzle exit to the cylinder surface is $L/D = 1.5$. Within this distance ($L/D = 1.5$), the increase in the width of the jet flow is not significant before the jet flow hits the rotating cylinder. Hence, the nozzle distance L/D has only a negligible effect on the results [8]. The grid system shown in Fig. 2 seems to be adequate for all of the parameters that were investigated in the present study.

The results of streamlines and isotherms for $Re_j = 500$ under various rotation Reynolds numbers are shown in Fig. 3. Figure 3(a) reveals the streamlines when the cylinder is stationary ($Re_\omega = 0$). For convenience, the streamlines of the jet flow are represented by solid curves, while those of the induced flow are denoted by dashed curves. In Fig. 3, 11 solid curves are employed for the jet flow such that the increment of the stream function is $\Delta\psi = 0.03$ due to the particular nozzle width $E/D = 0.3$ (see equation (23)). This renders the stream functions of these 11 streamlines expressible as $\psi = \psi_0 + i\Delta\psi$, where $i = -5, \ldots, -1, 0, 1, \ldots, 5$. Such an increment for streamlines along with the increment $\Delta\theta = 0.1$ for isotherms will be used for all of the streamlines and isotherms in the present paper.

From Fig. 3(a), the jet flow is seen to separate into two branches after hitting the cylinder. The upper branch eventually heads straight in a direction near $\phi = 45°$. Due to symmetry, the lower branch flows straight near $\phi = 315°$. Like undisturbed free jets, both branches have decreasing velocity and increasing

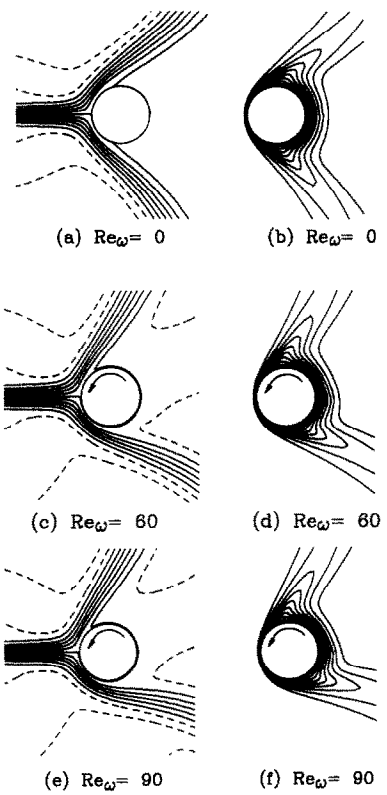

FIG. 3. Streamlines and isotherms for $Re_j = 500$ and various rotation Reynolds numbers based on the two-hump mode.

width along their flow directions. In addition, the velocity near the cylinder is very small owing to the existence of a boundary layer. This agrees with the physical reasoning. As expected, there is a stagnation point on the cylinder surface at $\phi = 180°$. However, the flow behind the cylinder is essentially quiescent. No vortex shedding can be found. Figure 3(b) shows the isotherms based on the flow field of Fig. 3(a). From Fig. 3(b), it can be seen that the temperature gradient is quite large near the stagnation point. On the lee side of the cylinder, however, heat conduction dominates the heat transfer due to the quiescent air. In regions near $\phi = 45°$ and 315°, the jet flow brings the hot air from the cylinder surface to the downstream region. As a result, high temperature regions develop along each of the jet branches such that sharp humps on the isotherms are found there. The humps give rise to small temperature gradients and thus decrease the Nusselt number. This will be discussed later.

When the rotation Reynolds number Re_ω increases from 0 to 60, the streamlines and the associated isotherms transit from Figs. 3(a) and (b) to Figs. 3(c) and (d), respectively. Due to the rotation of the cylinder, the stream function at the center of the nozzle exit is no longer zero ($\psi_0 \neq 0$). Hence, the streamline $\psi = 0$ (representing the cylinder surface) does not necessarily belong to the family of streamlines with the increment $\Delta\psi = 0.03$. From Fig. 3(c), one sees that the sixth streamline of the jet flow is wound

around the cylinder due to the non-slip condition on the surface of the rotating cylinder, while the other streamlines are still separated into two branches. Figure 3(c) indicates also that the upper branch of the jet flow is retarded by the rotating cylinder such that the separation point slightly moves upstream. In contrast, the separation point of the lower branch moves downstream owing to the aid of the rotating cylinder. The humps of the isotherms thus move counterclockwise as can be seen from Fig. 3(d). Such a characteristic does not change when the rotation Reynolds number further increases to $Re_\omega = 90$ (see Figs. 3(e) and (f)).

Generally speaking, the solution of a lower Re_ω makes a good initial guess for the solution of a higher Re_ω. In the present computations, the solution for $Re_\omega = 100$ (based on $Re_j = 500$) was attempted by starting the numerical procedure from the results of $Re_\omega = 90$ (i.e. Figs. 3(e) and (f)) as usual. However, the solution convergence was found to be very difficult. After numerous iterations, the solution eventually converged to the streamlines and isotherms as shown in Figs. 4(c) and (d). Figure 4(c) reveals that the lower branch of the jet flow winds around the cylinder and meets the upper branch again on the top of the cylinder. Such a situation diffuses the streamlines of the lower branch. As a result, each isotherm in Fig. 4(d) has only a single hump. Their lower humps are all gone. This characteristic can also be observed in the solutions of higher rotation Reynolds numbers such as $Re_\omega = 300$ in Figs. 4(e) and (f) and $Re_\omega = 500$ in Figs. 4(g) and (h).

It is interesting to note that dual solutions do exist in the present problem in a range of rotation Reynolds numbers under the parameter of $Re_j = 500$. To clarify this point, the solution procedure for $Re_\omega = 90$ is performed once again by using the streamlines and isotherms of $Re_\omega = 100$ (Figs. 4(c) and (d)) as the initial guess. The computations seem quite easy to arrive at the solution shown in Figs. 4(a) and (b) that possess only one-hump isotherms. This implies that the solution for $Re_\omega = 90$ will either converge to Figs. 3(e) and (f) or to Figs. 4(a) and (b), depending on the initial guess. For convenience, the two solution modes will be referred to as the 'two-hump mode' and the 'one-hump mode' in the present paper.

It should be noted here that the Navier–Stokes equation is highly nonlinear, especially when the magnitude of the nonlinear inertia term is large. Hence, it is not surprising to find dual solutions for high Reynolds numbers. As pointed out by Temam [11], the Navier–Stokes equation has only been proved to possess unique solution under the assumptions that the viscosity is sufficiently large, or that the given forces and boundary values are sufficiently small. It is expected that otherwise the solution is not unique. This has been proved by Iudovich [12, 13], Rabinowitz [14], Velte [15] and many others. In fact, dual solutions for steady fluid flow and heat transfer problems have also been found in many experiments [16, 17]. Mathematically, there could be more than two solutions for a nonlinear problem. However, only two of them were detected in the present study.

Figure 5(a) shows the local Nusselt number $Nu(\phi)$ for $Re_j = 500$ subject to the two-hump mode ($0 \leqslant Re_\omega \leqslant 90$). The Nusselt numbers for $Re_j = 500$ dealing with the one-hump mode ($90 \leqslant Re_\omega \leqslant 500$) are presented in Fig. 5(b). Note that the stagnation point is near $\phi = 180°$ for most rotation Reynolds numbers that were investigated. The upper branch of the jet flow goes from the stagnation point toward $\phi = 0$, while the lower branch flows toward $\phi = 360°$. From the Nusselt curves on Fig. 5(a), a maximum at $\phi = 180°$ and two minimums near $\phi = 80°$ and 280° are observable for the case of $Re_\omega = 0$. The maximum

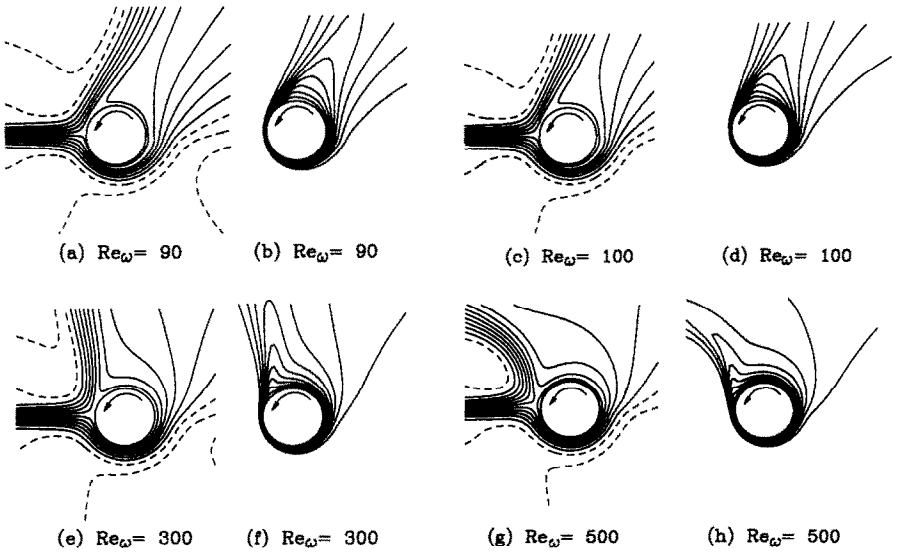

FIG. 4. Streamlines and isotherms for $Re_j = 500$ and various rotation Reynolds numbers based on the one-hump mode.

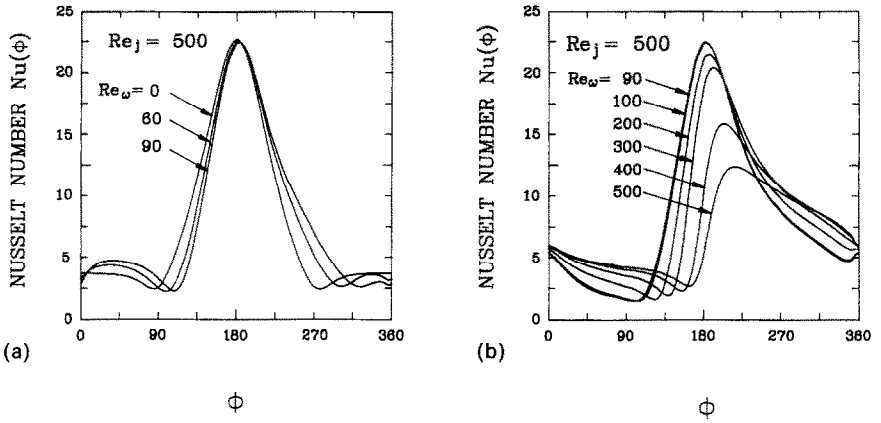

FIG. 5. (a) Local Nusselt number for $Re_j = 500$ based on the two-hump mode. (b) Local Nusselt number for $Re_j = 500$ based on the one-hump mode.

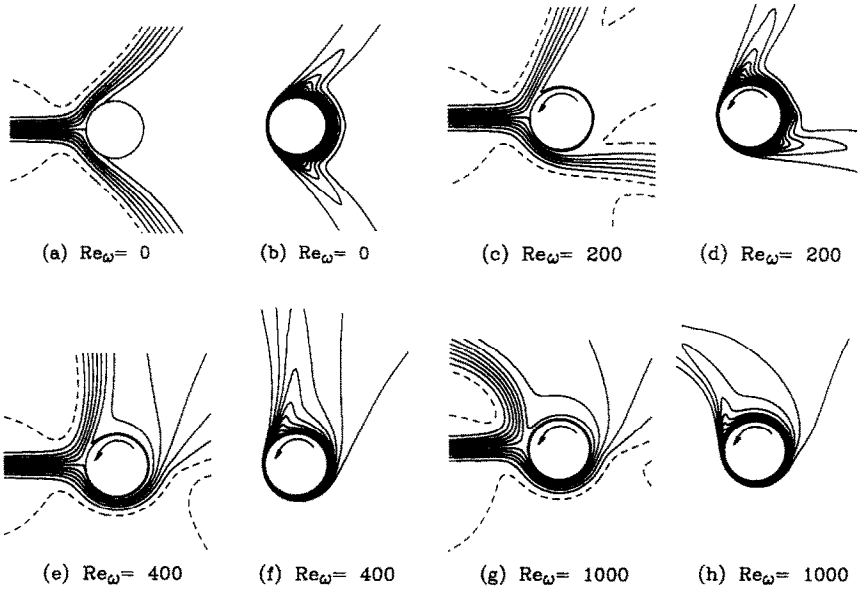

FIG. 6. Streamlines and isotherms for $Re_j = 1000$ and various rotation Reynolds numbers.

and the minimums are, respectively, caused by the stagnation point and the humps on the isotherms, as shown in Fig. 3. As mentioned earlier, the stagnation point and the separation points all move counterclockwise, when the rotation speed of the cylinder increases. Hence, from Fig. 5(a), one can see that the maximum and the minimums of the Nusselt curve all move to the right as Re_ω increases. Similar phenomena can be found in Fig. 5(b) for the one-hump mode except for its missing hump on the lower branch. Figure 5(b) indicates also that the maximum Nusselt number at the 'stagnation point' decreases significantly when the rotation Reynolds number increases. This is attributed to a layer of dead air wound around the cylinder surface due to the non-slip condition. Hence, a more uniform heat transfer rate can be achieved by rotating the cylinder.

Figures 6 and 7 show the streamlines, the isotherms and the local Nusselt numbers for $Re_j = 1000$ under various rotation Reynolds numbers. Similar infor-

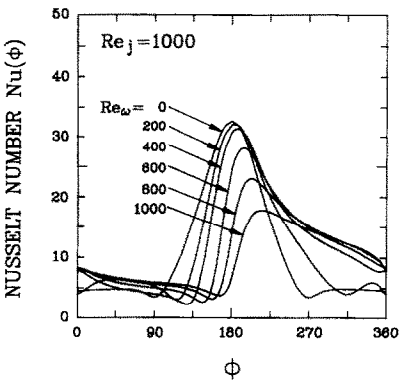

FIG. 7. Local Nusselt number for $Re_j = 1000$ and various rotation Reynolds numbers.

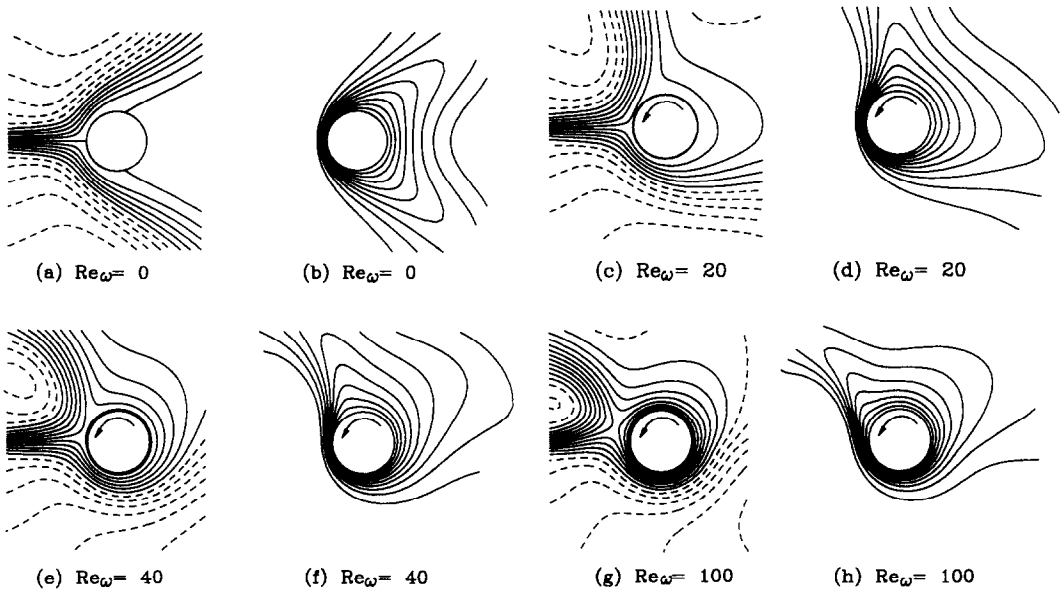

FIG. 8. Streamlines and isotherms for $Re_j = 100$ and various rotation Reynolds numbers.

mation was provided in Figs. 8 and 9 for $Re_j = 100$. These results reveal that the physical phenomena of $Re_j = 100$ and $Re_j = 1000$ are essentially the same as that of $Re_j = 500$. A jump between the two-hump and the one-hump modes is also found in the case of $Re_j = 1000$ near $Re_\omega = 300$. It, however, is not clear for a jet Reynolds number Re_j as small as 100.

Finally, the average Nusselt numbers for $Re_j = 100$, 500 and 1000 are plotted in Fig. 10 with the abscissa $\lambda = Re_\omega/Re_j$. It appears from Fig. 10 that increasing the jet Reynolds number (Re_j) would significantly increase the Nusselt number. As mentioned earlier, rotating a cylinder in a quiescent air will always decrease the heat transfer as long as the flow does not transit to three-dimensional secondary flow [3, 4]. Thus, for a jet Reynolds number as small as 100, it is not surprising to see a monotonically decreasing average Nusselt number ($\overline{Nu}$) from Fig. 10 for an increasing rotation speed. As demonstrated in Figs. 3, 4 and 6, there are two solution modes for the cases of $Re_j = 500$ and 1000. When the rotation Reynolds number is small, the two-hump solution mode prevails. Under such a situation, the rotation Reynolds number does not show great influence on the upper branch of the jet flow, while it depresses the flow separation on the lower branch. As a result, increasing the rotation speed of the cylinder enhances the average heat transfer as long as the two-hump mode can be maintained. This trend is reversed once the solution jumps to the one-hump mode for high rotation Reynolds numbers as observable from Fig. 10. Like the transition from laminar flow to turbulent flow, the jump from the two-hump mode to the one-hump mode depends on the flow instability. Unfortunately, the only available experiment [8] dealing with rotating cylinder and jet cooling is restricted to the parameters $0.02 \leqslant E/D \leqslant 0.1$, $10^4 \leqslant Gr \leqslant 10^8$, $10^5 \leqslant Re_j \leqslant 10^6$ and $5000 \leqslant Re_\omega \leqslant 70\,000$ such that

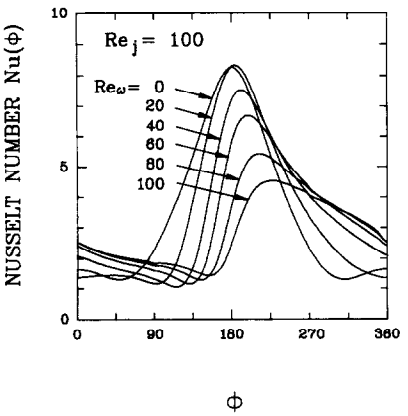

FIG. 9. Local Nusselt number for $Re_j = 100$ and various rotation Reynolds numbers.

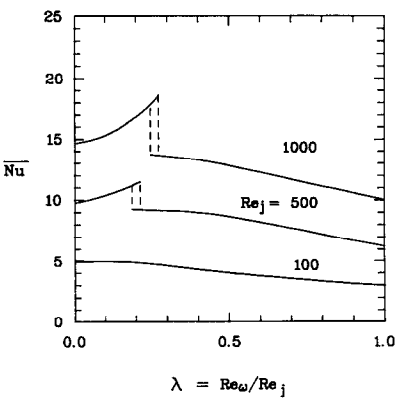

FIG. 10. Average Nusselt number for various rotation speed at $Re_j = 100$, 500 and 1000.

transition between the two solution modes could not be properly observed. More experiments are needed to verify this interesting physical phenomenon.

CONCLUSION

The purpose of the present investigation is to study the flow structure and heat transfer on a rotating cylinder cooled with an air jet. An irregular computational domain is employed to properly handle the jet flow before and after hitting the cylinder. The solutions reveal that there are two solution modes in the present problem. For slow rotation speeds, the jet flow is separated into two branches after hitting the cylinder. Each branch possesses a separation point. The rotating cylinder accelerates one of the jet branches such that the separation point moves downstream, while the other separation point receives no significant influence. As a result, the overall heat transfer is enhanced. Unlike the case with cross-flow, no vortex shedding was found behind the cylinder. The other solution mode occurs when a layer of dead air is wound around the cylinder at high rotation Reynolds number. This situation achieves a more uniform heat transfer rate, although the overall heat transfer is depressed. Dual solutions were found in a range of rotation Reynolds numbers for both cases of $Re_j = 500$ and 1000. This implies that, like transition from laminar flow to turbulent flow, the solution could jump back and forth between the two solution modes depending on the flow instability. However, smooth transition between the two solution modes is found for a jet Reynolds number as small as 100. More experiments are needed to verify this physical phenomenon.

Acknowledgement—The authors wish to express their appreciation to Mr S. S. Wang for his assistance in preparing Fig. 5(a).

REFERENCES

1. J. T. Anderson and O. A. Saunders, Convection from an isolated heated horizontal cylinder rotating about its axis, *Proc. R. Soc. Lond.* **A217,** 555–562 (1953).
2. D. Dropkin and A. Carmi, Natural-convection heat transfer from a horizontal cylinder rotating in air, *Trans. ASME* **79,** 741–749 (1957).
3. G. A. Etemad, Free-convection heat transfer from a rotating horizontal cylinder to ambient air with interferometric study of flow, *Trans. ASME* **77,** 1283–1289 (1955).
4. B. Farouk and K. S. Ball, Convective flows around a rotating isothermal cylinder, *Int. J. Heat Mass Transfer* **28,** 1921–1935 (1985).
5. W. M. Kays and I. S. Bjorklund, Heat transfer from a rotating cylinder with and without crossflow, *Trans. ASME* **80,** 70–78 (1958).
6. J. Jones, D. Poulikakos and J. Orozco, Mixed convection from a rotating horizontal heated cylinder placed in a low-speed wind tunnel, *Int. J. Heat Fluid Flow* **9,** 165–173 (1988).
7. H. M. Badr and S. C. R. Dennis, Laminar forced convection from a rotating cylinder, *Int. J. Heat Mass Transfer* **28,** 253–264 (1985).
8. X. Zhang, W. Li and L. Wei, A study of heat transfer associated with the cooling of a horizontal rotating cylinder using air jet flow, *Proc. 8th Int. Heat Transfer Conf.* **3,** 1265–1270 (1986).
9. K. Hsu and S. L. Lee, A numerical technique for two-dimensional grid generation with grid control at all of the boundaries, *J. Comput. Phys.* **96,** 451–469 (1991).
10. S. L. Lee, Weighting function scheme and its application on multidimensional conservation equations, *Int. J. Heat Mass Transfer* **32,** 2065–2073 (1989).
11. R. Temam, *Navier–Stokes Equations*, Chap. II, Section 4. Bifurcation Theory and Non-Uniqueness Results, pp. 223–246. North-Holland Publishing, Amsterdam (1979).
12. V. I. Iudovich, Secondary flows and fluid instability between rotating cylinders, *PMM* **30,** 688–698 (1966).
13. V. I. Iudovich, On the origin of convection, *PMM* **30,** 1000–1005 (1966).
14. P. H. Rabinowitz, Existence and nonuniqueness of rectangular solutions of the Benard Problem, *Archs ration. Mech. Analysis* **29,** 32–57 (1968).
15. W. Velte, Stabilitatsverhalten und verzweigung stationarer losungen der Navier–Stokesschen gleichungen, *Archs ration. Mech. Analysis* **16,** 97–125 (1964).
16. M. J. Bagshaw, J. D. Hunt and R. M. Jordan, Heat line formation in a roll caster, *Appl. Scient. Res.* **44,** 161–174 (1987).
17. F. B. Hsiao, C. F. Liu and Z. Tang, Aerodynamic performance and flow structure studies of a low Reynolds number airfoil, *AIAA J.* **27,** 129–137 (1989).